

MODELLING PARTICLE DEAGGLOMERATION IN A BATCH HOMOGENIZER USING FULL CFD AND MECHANISTIC MODELS

Radosław Krzosa¹, Krzysztof Wojtas¹, Jakub Golec¹, Łukasz Makowski¹,
Wojciech Orciuch¹, Radosław Adamek²

¹Warsaw University of Technology, Faculty of Chemical and Process Engineering, ul. Waryńskiego 1,
00-645 Warsaw, Poland

²ICHEMAD–Profarb, ul. Chorzowska 117, 44–100 Gliwice, Poland

Modelling of titanium dioxide deagglomeration in the mixing tank equipped with a high shear impeller is presented in this study. A combination of computational fluid dynamics with population balance was applied for prediction of the final particle size. Two approaches are presented to solve population balance equations. In the first one, a complete population balance breakage kinetics were implemented in the CFD code to simulate size changes in every numerical cell in the computational domain. The second approach uses flow field and properties of turbulence to construct a mechanistic model of suspension flow in the system. Such approach can be considered as an attractive alternative to CFD simulations, because it allows to greatly reduce time required to obtain the results, i.e., the final particle size distribution of the product. Based on experiments shattering breakage mechanism was identified. A comparison of the mechanistic model and full CFD does not deviate from each other. Therefore the application of a much faster mechanistic model has comparable accuracy with full CFD. The model of particle deagglomeration does not predict a very fast initial drop of particle size, observed in the experiment, but it can predict, with acceptable accuracy, the final particle size of the product.

Keywords: population balance, titanium dioxide, CFD, breakup, high shear impeller

1. INTRODUCTION

Titanium dioxide has many specific properties that make it valuable and important in many branches of science and industry. This substance has a high value of refractive index and is known to be of chemical and mechanical resistance that makes it useful in the optical industry (Mandzy et al., 2005). Because titanium dioxide has photocatalytic properties, it can be used in hydrogen production reactions, decomposition of organic compounds and sterilization (Fujishima et al., 2000). Owing to specific properties titanium dioxide can be used in manufacturing of antimicrobial coatings (Chung et al., 2008), super-hydrophilic coatings (Yu et al., 2001) and nanocomposite films (Hass, 1952). Due to its whiteness and opacity, it is commonly used as a pigment in the paint (Middlemas et al., 2015), food (Meacock et al., 1997) and cosmetic industry (Weir et al., 2012). Considering all mentioned applications, a study on the preparation process of this material is important to design more efficient devices.

* Corresponding author, e-mail: lukasz.makowski.ichip@pw.edu.pl

<https://journals.pan.pl/cpe>



The properties of the substance do not only result from its composition but also from its preparation method (Rodgers et al., 2009). The two most popular methods used in the industrial scale of titanium dioxide powder manufacturing are sulfide and chloride methods (Gázquez et al., 2014; Reck and Richards, 1999). The production method may influence substance properties, e.g., by affecting the particle composition of the product. Composition of solid phase from fluid consist of several stages (Boverhof et al., 2015). The first one is a nucleation process, in which primary particles are created from continuous phase. In the second stage those particles chemically bond with each other. Those clusters of particles are named aggregates. In the last step, aggregates can collide and create larger clusters, named agglomerates (Hansen et al., 1998). Connection between aggregates in agglomerate is a result of two forces acting between them. The first is the Van der Waals attraction force that holds particles, and the second is the electrostatic repulsion force that is the result of electrostatic double layer on a surface of the particles (Shamlou and Titchener-Hooker, 1993). Also primary particles can stick to one another via adhesion forces and create agglomerate of primary particles. The bond between agglomerate compounds can be easily broken via hydrodynamic stresses, whereas breakage of aggregate bonds as a result of those stresses is not possible (Özcan-Taşkın et al., 2009; Xie et al., 2007).

A deagglomeration process consists of breaking bonds between agglomerate compounds. This process can be carried out in various type of devices, such as mixing tanks equipped with high shear impeller (Martínez-de Jesús et al., 2018; Unadkat et al., 2011; Zhang et al., 2012), rotor stator systems (Atiemo-Obeng and Calabrese, 2004; Bałdyga et al., 2007; Özcan-Taşkın et al., 2016; Kamaly et al., 2017; Özcan-Taşkın et al., 2009), ball mills (Gajović et al., 2001; Sen et al., 1999), pressure nozzles (Bałdyga et al., 2008b, 2007; Gavi et al., 2018; Xie et al., 2008) and ultrasonication systems (Bałdyga et al., 2008a; Mandzy et al., 2005). Performance characteristics of these devices are presented in (Atiemo-Obeng and Calabrese, 2004).

In this work, the process of titanium dioxide deagglomeration was investigated. In the experimental part, particle size evolution was investigated for the rotation speed of an impeller in a range from 500 rpm to 1200 rpm. The deagglomeration process was carried out using a high shear impeller. In the modelling part, computational fluid dynamics and population balance methods are combined to reconstruct the process and find the procedure that allowed the prediction of the final particle size. Two approaches are used. In the first one, population balance equations were implemented into CFD code. In the second approach, CFD results were used to create a mechanistic model of suspension flow.

2. EXPERIMENTAL

The process of titanium dioxide deagglomeration was carried out in a cylindrical tank without baffles, equipped with the high shear impeller. The configuration reflects the design used in large scale manufacture. Both the tank and impeller are presented in Figure 1. The tank diameter was equal to $T = 240$ mm, liquid height was equal to $H = 115$ mm. The tank had a rounded bottom edge ($R = 10$ mm) to prevent creation of a dead zone in this region. The impeller diameter was equal to $D = 157$ mm. The impeller used in experiments was a flat disc with cuts on its edge which increase breakage of a particles, and cylindrical holes to increase circulation of the suspension in the system. The holes were placed on circumference of diameter $D_2 = 70$ mm. The diameter of holes was equal to $d = 16$ mm. Samples were collected from the same place in the tank, 10 mm above the impeller level, during the process without stopping the impeller.

The samples were diluted with demineralized water before further measurements. The initial mean size L_{43} of the titanium dioxide particles was 21 μm . The titanium dioxide powder used in the experiment was an industrial grade. It had a rutile structure (density $4260 \text{ kg}\cdot\text{m}^{-3}$). The suspension was made of demineralised water of conductance not greater than 0.05 μS . The concentration of the powder in the suspension was 40% of the mass. Tap water flow was used as a coolant in the tank jacket.

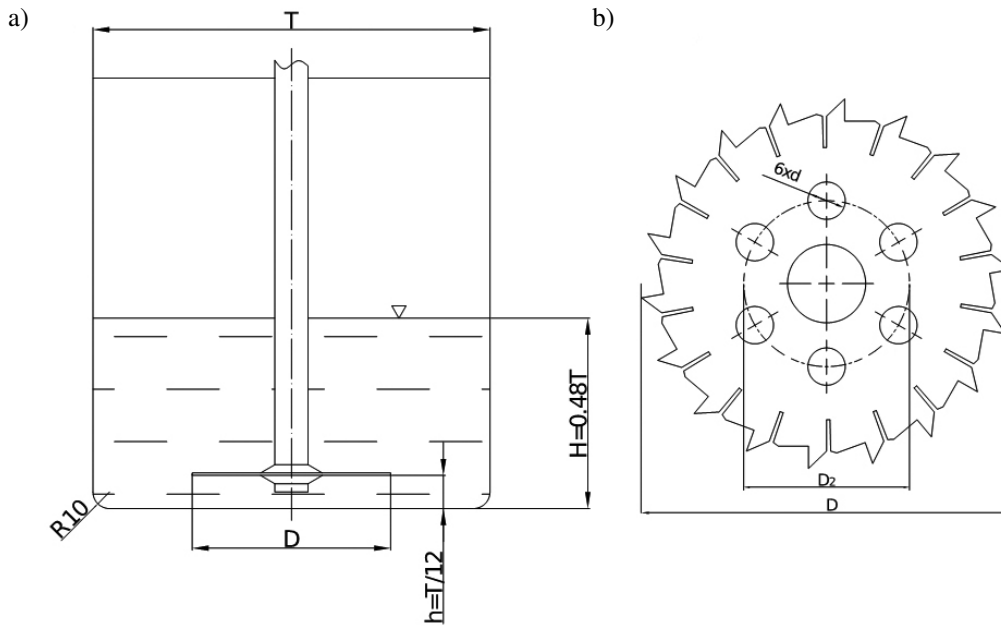


Fig. 1. Tank and impeller geometry

The particle size distribution was measured with the Beckman&Coulter LS 13 320 particle size analyser. The device uses laser diffraction (LD) and Polarisation Intensity Differential Scattering (PIDS) techniques to measure particle sizes in range from 40 nm to 2000 μm . The PIDS technology uses three wavelengths, in two polarisations each, to measure particle sizes. The optical model for titanium dioxide used in this study for wavelengths required in the PIDS measurements is presented in Table 1. The initial particle size distribution of titanium dioxide is presented in Fig. 2. Five samples were taken from the batch to average initial particle size distribution. The figure shows that the powder consists of two populations of particles, first, with a mean size of 4 μm and a second of 30 μm .

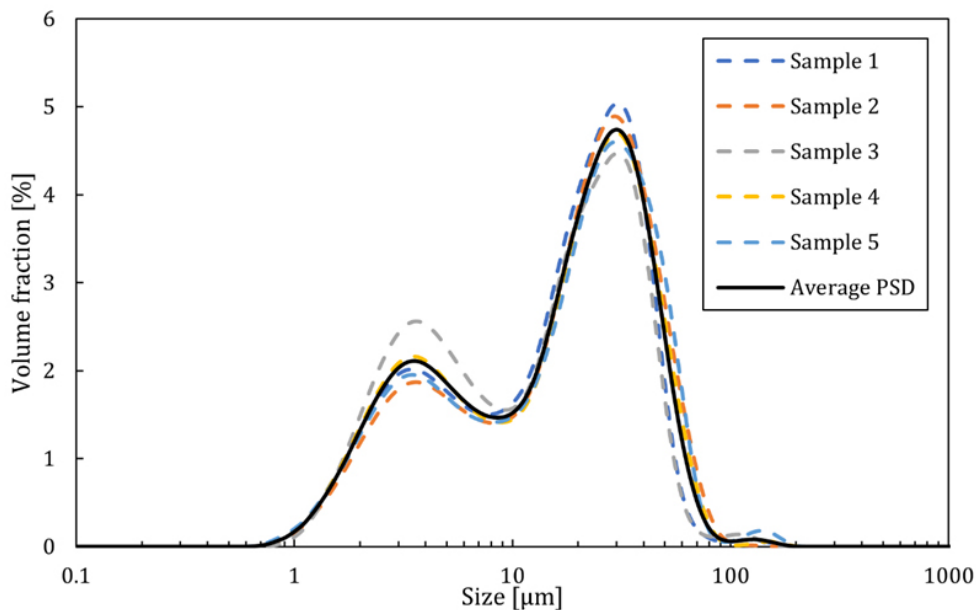


Fig. 2. Initial particle size distribution

Table 1. Optical model of TiO₂

Wavelength [nm]	Real part of refractive index	Imaginary part of refractive index
450	3.14	0
600	2.90	0
900	2.77	0

3. PROCESS MODELLING

3.1. Simulation

Numerical mesh for the tank geometry (Fig. 1) was created using ANSYS Fluent Meshing 20R1. 1 500 000 poly-hexcore cells were created in total as a base mesh, which underwent further refinement for each analysed impeller speed. Several simulations were made to find mesh for which parameters were independent of number of mesh elements. In order to reconstruct liquid surface curvature (swirl) during the process, the $k-\varepsilon$ turbulence model together with volume of fluid (VOF) multiphase model were used. For low concentration of solid phase, rheology of the suspension can be approximate as a Newtonian fluid with viscosity expressed by an Einstein equation (Yang et al., 2001). For higher values of solid-phase concentration, a study on viscosity performed by Mikulášek et al. (1997) and Yang et al. (2001) presented several models which can approximate the rheological behaviour of titanium dioxide suspensions. In our case to represent the rheological behaviour of the suspension, the Carreau rheology model was applied. In this model, the relation between apparent viscosity and shear rate is expressed by the following equation:

$$\mu = \mu_{\infty} + (\mu_0 - \mu_{\infty}) \left[1 + (\lambda \dot{\gamma})^2 \right]^{\frac{n-1}{2}} \quad (1)$$

where $\dot{\gamma}$ [s⁻¹] is the shear rate, λ [s] is the relaxation time, μ_{∞} [Pa·s] is the apparent viscosity at infinite shear rate, μ_0 [Pa·s] is the apparent viscosity at zero shear rate and n [-] is the flow behaviour index. The model constants used in this work are presented in Table 2. Experiments were carried out on titanium dioxide particles after deagglomeration on Anton Paar MCR 302 using plate-plate system and coaxial cylinders system. The flow curve obtained from the measurement corresponds to a rheological behaviour of the suspension used in this study.

Table 2. Model constants

λ [s]	μ_0 [Pa·s]	μ_{∞} [Pa·s]	n [-]
1.73	14.09	0.11	0.1

3.2. Population balance

The population balance equation that describes the change of particle size distribution was introduced by Randolph and Larson, (1962). In the case when only breakage of particles occurs in the system, the population balance equation can be expressed as described by Bałdyga et al., (2007):

$$\frac{\partial f(L, \mathbf{x}, t)}{\partial t} + \sum_{i=0}^3 \frac{\partial [u_{p,i}(L, \mathbf{x}, t) f(L, \mathbf{x}, t)]}{\partial x_i} + \frac{\partial [G(L, \mathbf{x}, t) f(L, \mathbf{x}, t)]}{\partial L} = B^b(L, \mathbf{x}, t) + D^b(L, \mathbf{x}, t) \quad (2)$$

where $f(L, \mathbf{x}, t)$ is number of particles of characteristic length L , position vector \mathbf{x} and time t . In the convective term, $u_{p,i}$ is the velocity of particles in i direction, G is the linear growth rate function of

particles. In the case when only breakage occurs in the system, this function is equal to zero. The right-hand side of Eq. (2) represents source terms. The birth function B^b describes appearance of new particles in the system due to breakage, whereas the death function D^b describes loss of particles due to breakage. The birth function can be expressed as follows:

$$B^b(L, \mathbf{x}, t) = \int_L^\infty \Gamma(\lambda) b(L|\lambda) f(\lambda, \mathbf{x}, t) d\lambda \quad (3)$$

where $\Gamma(\lambda)$ is the breakage kernel and describes frequency of breakage events in the system, $b(L|\lambda)$ is the fragment size distribution function and describes number of particles of size L that are created by breakage of a large agglomerate of size λ . The death function can be expressed by:

$$D^b(L, \mathbf{x}, t) = \Gamma(L) f(L, \mathbf{x}, t) \quad (4)$$

The fragment distribution function depends on the included breakage mechanism, for example see Marchisio et al. (2003). In this work, shattering was identified as the main, dominating mechanism of particle breakage. It is clearly visible in the Fig. 3. It shows the particle size distribution for different times of deagglomeration for 500 rpm.

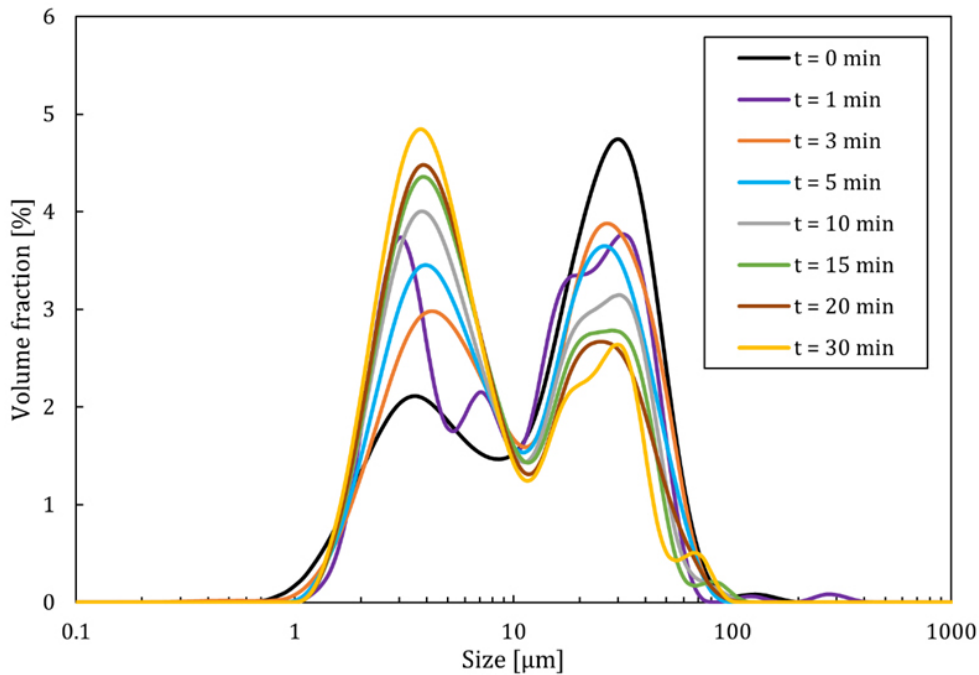


Fig. 3. Particle size distribution change in time for impeller speed 500 rpm

The fragment distribution function for the shattering mechanism is expressed by:

$$b(L|\lambda) = N(\lambda) \cdot \delta(L - L_a) \quad (5)$$

where L_a is the size of aggregates, equal $L_a = 4 \mu\text{m}$. $N(\lambda)$ is the number of aggregates in an agglomerate of size λ . This value can be estimated from the following equation (Bałdyga et al., 2007):

$$N(\lambda) = \left(\frac{k_v}{k_{va}} \right)^{\frac{D_f}{3}} \left(\frac{\lambda}{L_a} \right)^{D_f} \quad (6)$$

where D_f is the fractal dimension, k_v and k_{va} are the volume shape factors of agglomerates and aggregates respectively. The values of these parameters are: $D_f = 2.85$, $k_v = k_{va} = \pi/6$. The parameters were taken

from another publication for similar material silicon oxide, described in (Bałdyga et al., 2008b). The breakage kernel used in this work includes the effect of mixing (turbulence) in the system. Based on the Kolmogorov turbulence spectrum the kernel is described in two cases: if particles are smaller than Kolmogorov length scale $L < \lambda_K$:

$$\Gamma(L) = \begin{cases} C_b \left(\frac{\varepsilon}{\nu}\right)^{1/2} & \text{if } \mu \left(\frac{\varepsilon}{\nu}\right)^{1/2} > \sigma \\ 0 & \text{if } \mu \left(\frac{\varepsilon}{\nu}\right)^{1/2} \leq \sigma \end{cases} \quad (7)$$

otherwise, if particles are larger than Kolmogorov length scale $L > \lambda_K$:

$$\Gamma(L) = \begin{cases} C_b \left(\frac{\varepsilon}{L^2}\right)^{1/3} & \text{if } \rho(\varepsilon L)^{1/3} > \sigma \\ 0 & \text{if } \rho(\varepsilon L)^{1/3} \leq \sigma \end{cases} \quad (8)$$

where ε [m²/s³] is the turbulence energy dissipation rate, μ [Pa·s] is the dynamic viscosity of the continuous phase, equals $\mu = 1.003 \cdot 10^{-3}$ Pa·s, ν [m²/s] is the kinematic viscosity of the medium, ρ [kg/m³] is the density of the medium, equal: $\rho = 998.2$ kg/m³, σ [Pa] is the tensile strength of the agglomerate and C_b [-] is the breakage constant.

Eqs. (6) and (7) show that breakage of the particles occurs only when hydrodynamic stresses, which are generated in the suspension, have a higher value than the tensile strength of the agglomerate. This strength is the result of two existing forces: Van der Waals attraction and electrostatic repulsion. For fractal aggregates, the tensile strength can be found from the equation (Tang et al., 2001):

$$\sigma = 1.1 \frac{1 - \epsilon}{\epsilon} \frac{F}{L_a^2} \quad (9)$$

where ϵ [-] is the porosity of an aggregate, F [N] is the force between particles and was calculated from:

$$F = F_A + F_R \quad (10)$$

where F_A [N] is the Van der Waals attraction force and F_R [N] is the electrostatic repulsion force. In this case only the attraction force was involved and was calculated using the following formula:

$$F_A = \frac{HaL_0}{48H^2} \quad (11)$$

where Ha [J] is the Hamaker constant, is equal $Ha = 5 \cdot 10^{-21}$ J, L_0 [m] is the size of primary particles and is equal to: $L_0 = 20$ nm, H [m] is the separation or surface to surface distance, its value was taken as: $H = 1$ nm. The model parameters were taken from model presented in: (Bałdyga et al., 2008b) for silicon oxide, a similar material. The same approach was applied in (Krzosa et al., 2021). The porosity of an aggregate can be calculated as:

$$\epsilon(L) = 1 - \frac{D_f}{3} \frac{k_v \left(\frac{D_f}{3}\right)^{-1}}{k_{va} \left(\frac{D_f}{3}\right)^{-1}} \left(\frac{L}{L_a}\right)^{D_f-3} \quad (12)$$

3.3. Mechanistic model

The model of suspension flow in the system assumes that every fluid element circulates in the tank in the same way. Based on steady state simulations, the tank was divided into three regions characterized by different values of energy dissipation rate. Let us define here the parameter ε_{cr} , which is a value of turbulent

energy dissipation rate that initiates the deagglomeration process. Below this value, hydrodynamic stresses cannot break agglomerate bonds. In region I, energy dissipation rate was greater than the average value on the whole tank. In region II, energy dissipation rate was in range from critical value ε_{cr} to average on the whole system. In the rest of the domain, named as region III, the deagglomeration process does not occur due to not sufficient hydrodynamic stresses not being sufficient enough in this zone. The flow of the suspension is illustrated in Fig. 4. The red arrow represents flow in region I, the orange arrow represent flow in region II and the green arrow represent flow in region III. The arrows represent the movement of the suspension in the tank, as assumed in the model. In the real process, the circulation of the suspension is mostly tangential with a weak axial flow. Population balance, i.e., the course of the deagglomeration process, was solved using DQMOM method (Marchisio and Fox, 2005). Particle size distribution was approximated via three Dirac deltas. Residence time in each zone was calculated based on the volume of the zone and suspension flow near the impeller. Parameter C_b that was found to be the best fit the experiment, was equal to $C_b = 1 \times 10^{-6}$.

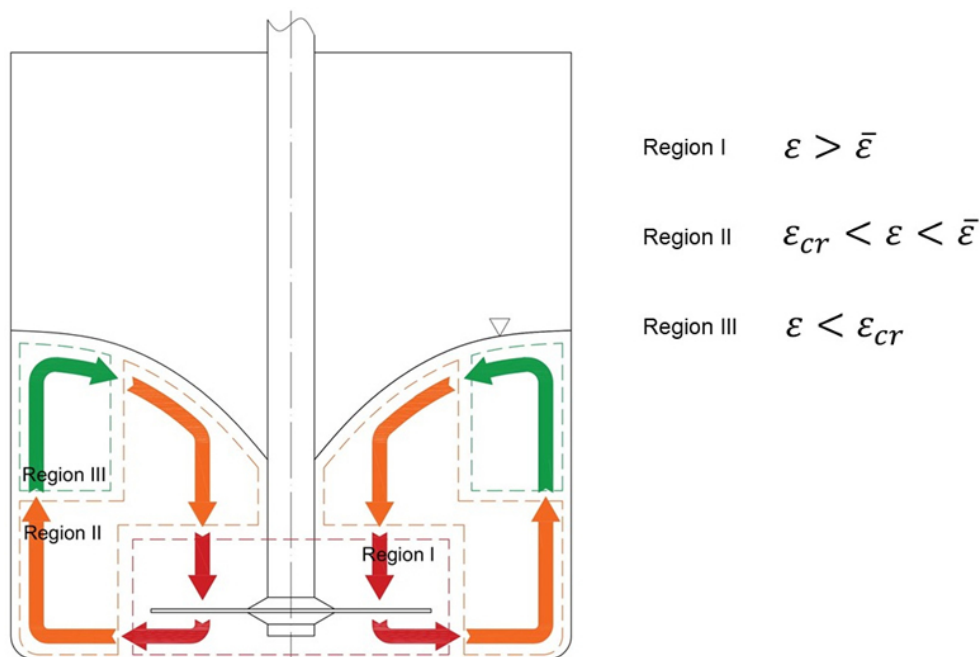


Fig. 4. Path of fluid elements through regions of different turbulent energy dissipation in the tank

In order to validate the mechanistic model, the population balance was solved together with computational fluid dynamics, using transient computations to predict the population balance evolution. The quadrature method of moments (QMOM) (McGraw, 1997) was implemented in a custom CFD code, and six moments were tracked in space and time.

4. RESULTS

Results for the volume fraction of suspension ϕ [-] are presented in Fig. 5. The figure shows that for the rotational speed in the range from 800 rpm to 1200 rpm, liquid surface deformation is so strong that air bubbles are dispersed in the suspension. This phenomenon is connected with strong circulations that are generated by the impeller at high rotational speeds. It suggests that for a high rotational speed value, the impeller does not work with maximum efficiency. Analysis of these contours shows that for high rotational speed, only the tip of the impeller has contact with the suspension.

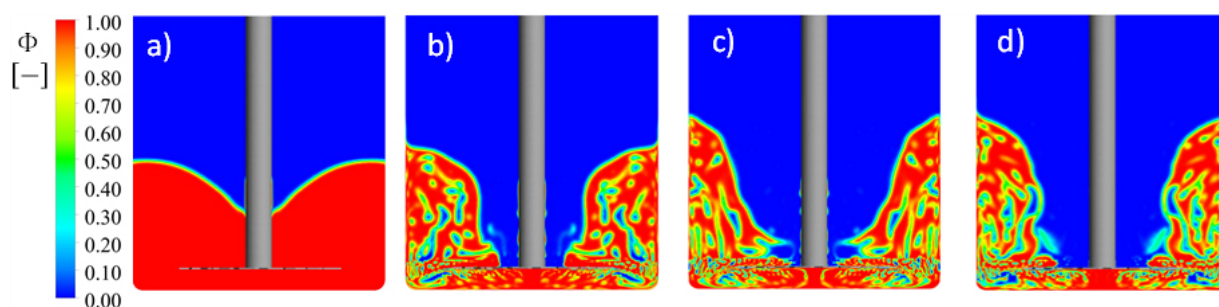


Fig. 5. Contours of liquid volume fraction for rotational speed of: a) 500 rpm, b) 800 rpm, c) 1000 rpm, and d) 1200 rpm

The results of apparent viscosity are presented in Fig. 6. Analysis of the contours indicates the creation of dead zones. In these zones, mixing is not as effective as in other zones. In these regions, circulation of suspension is lower. The existence of dead zones can decrease deagglomeration efficiency and leads to a less homogenous product. In the analysed cases, dead zones are located under the impeller for all rotational speeds. Of course, as the impeller speed increases, the volume of these zones decreases.

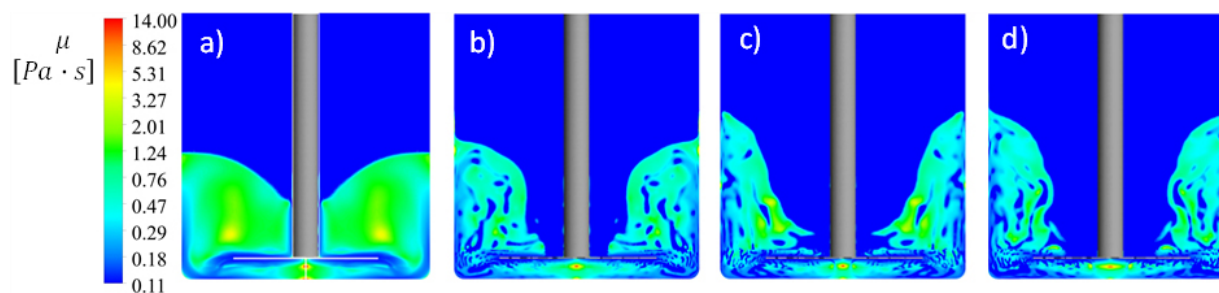


Fig. 6. Contours of apparent viscosity for rotational speed of: a) 500 rpm, b) 800 rpm, c) 1000 rpm, and d) 1200 rpm

The results for the turbulence energy dissipation rate are presented in Fig. 7. Results are presented using a logarithmic scale and show that the highest values of this parameter are generated near the impeller. In this region, hydrodynamic stresses have the highest value, and it is expected that deagglomeration is the most efficient. Also, there is a region of lower value of energy dissipation rate under the impeller hub. Connecting this with the higher apparent viscosity presented in Fig. 6, it suggest that in this region breakage of the particles will be less effective.

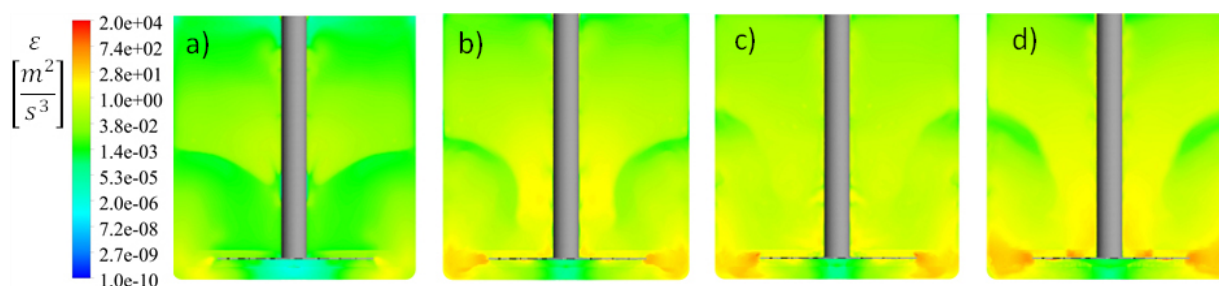


Fig. 7. Contours of turbulence dissipation rate for rotational speed of: a) 500 rpm, b) 800 rpm, c) 1000 rpm, and d) 1200 rpm, logarithmic scale

Based on the calculated fluid flow, the authors applied the population balance evolution using both the complete approach (CFD with QMOM) and the mechanistic model (with DQMOM). A comparison

between these two approaches is shown in Fig. 8. Mean particle size L_{43} was calculated based on the statistical moments, from the equation:

$$L_{43} = \frac{m_4}{m_3} \quad (13)$$

where m_3 and m_4 are moments of 3rd and 4th order respectively.

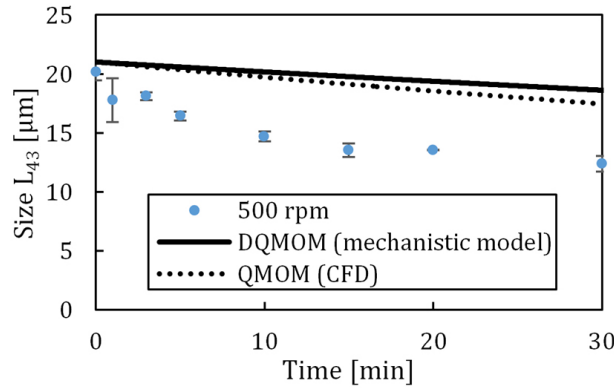


Fig. 8. Influence of time process on particle mean size for rotational speed of 500 rpm

The difference between both approaches is rather insignificant, visible only after about 15–20 minutes after the process started. Although the complete solution (CFD with QMOM) tends to give slightly more accurate results, it is important to note the limitations of the approach. The first one is the computational cost – it took several days just for one presented case (on AMD Ryzen 7 3700X CPU, 8 cores) to solve the transient simulations for scalars only (flow field was calculated for both models). If the process duration is longer or the number of analysed cases is larger, this makes the approach unfeasible in engineering applications. Moreover, to implement the method properly, extensive experience in programming of custom codes for CFD software is required. On the other hand, the CFD analysis allows observation in exactly which areas the deagglomeration of particles is taking place. Fig. 9 shows contours of the initial m_0 source term, ξ_0 , which can be interpreted as the regions of the particle deagglomeration.

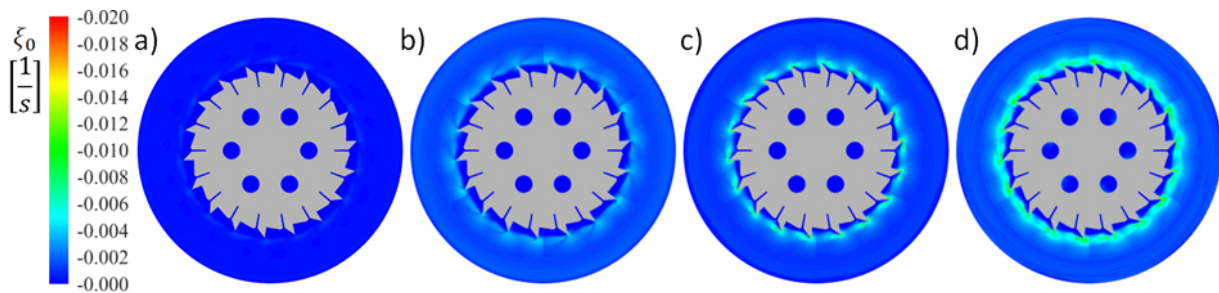


Fig. 9. Contours of the initial m_0 source term for rotational speed of: a) 500 rpm, b) 800 rpm, c) 1000 rpm, and d) 1200 rpm

One can see that the region where particle deagglomeration occurs is mainly around the impeller (Figs. 6 and 7) and of course, the higher the impeller rotational speed, the more pronounced the breakup. Since the deagglomeration occurs mainly at the tip of the impeller teeth, it is possible to optimize impeller design by attempting to maximize the initial value of the moment source term. However, this is not within the scope of this study.

Despite the valuable input from the complete CFD simulations, due to the mentioned limitations of the method, only the mechanistic model is further discussed in this work. Experimental results, compared with

the mechanistic model and DQMOM method, are presented in Fig. 10. Analysis of the result for rotational speed of 500 rpm, illustrated in Fig. 10a, shows that the model prediction deviates from experimental results. For this rotational speed, the turbulence of the flow may not be fully developed, whereas the equations, which describe breakage kinetics are formulated for fully turbulent flow – hydrodynamic stresses are calculated based on turbulence properties. For other rotational speeds, the final product size predicted by the mechanistic model, agrees with experimental data. At the beginning of the process, the modelling results are in poorer agreement with experimental data. The most probable reason is the occurrence of two breakage mechanisms that characterise the deagglomeration process: one causes rapid breakage of large agglomerates, and the other causes a slow size decrease of smaller ones. The evolution of mean particle size for rotational speed of 800, 1000 and 1200 rpm has a similar tendency. It may be related to the mentioned phenomenon, that the impeller does not work with full efficiency at these rotational speed values.

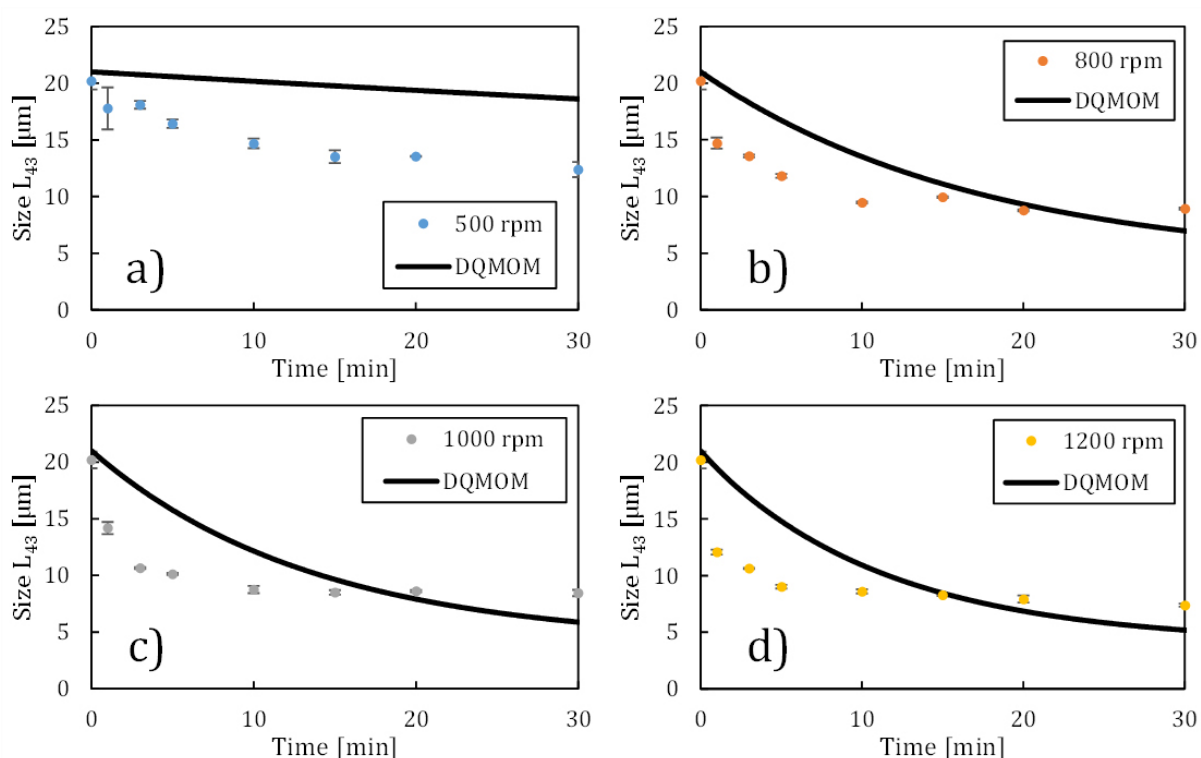


Fig. 10. Comparison of experimental results and mechanistic model for different rotational frequency: a) 500 rpm, b) 800 rpm, c) 1000 rpm, d) 1200 rpm

5. CONCLUSIONS

In this work, an experimental study of titanium dioxide deagglomeration in a mixing tank for four rotational speeds was performed. For every case, CFD simulation was performed, and population balance methods were applied to predict experimental results. Two approaches were used: mechanistic model and full CFD breakage modelling. The presented modelling method of deagglomeration allows to predict the process results with reasonable accuracy. The values of final product size obtained via modelling were comparable to experimental data. For higher rotational speeds, the model does not predict rapid particle size drop in the first minutes of the process. This phenomenon may be caused by the presence of a different mechanism of deagglomeration for larger particles in the first period of process. The applied CFD models allow to investigate the distributions of parameters in the system during the process. The presented analysis shows that under the impeller hub exists a dead zone that can cause inhomogeneities in the final product.

The mechanistic model of suspension flow allows obtain similar results as a complete combination of population balance implemented in CFD simulation. The time required to obtain population balance results from the mechanistic model was less than three minutes for every case (calculated on AMD Ryzen 7 3700X CPU using Matlab platform). The simplicity, speed, and accuracy of the method show that it is a good engineering tool combined with simple CFD simulations for designing processes or to compare different types of devices.

SYMBOLS

B^b	birth function, $\frac{\#}{\text{m}^3\text{m s}}$
$b(L \lambda)$	daughter size distribution, –
C_b	constant
D	impeller diameter, m
D^b	death function, $\frac{\#}{\text{m}^3\text{m s}}$
D_2	holes circle diameter, m
d	holes diameter, m
D_f	fractal dimension, –
f	particle number concentration, $\frac{\#}{\text{m}^3\text{m}}$
F	interacting forces, N
F_A	attraction forces, N
F_R	repulsion forces, N
G	linear growth rate, m/s
H	liquid level or surface to surface distance, m
Ha	Hamaker constant, J
k_v	shape factor of agglomerate, –
k_{va}	shape factor of aggregates, –
L	particle characteristic size, m
L_a	aggregate size, m
L_0	primary particles size, m
L_{43}	mean size of particles, m
m_3, m_4	moment of order 3 rd and 4 th , $\text{m}^3/\text{m}^3, \text{m}^4/\text{m}^3$
$N(\lambda)$	number of aggregates in agglomerate of size λ , –
n	flow index, –
R	rounding radius, m
t	time, s
T	tank diameter, m
\mathbf{x}	position vector, m

Greek symbols

γ	breakage kernel, s^{-1}
δ	dirac delta, –
ϵ	porosity, –
ε	turbulence energy dissipation rate, m^2/s^3
ε_{cr}	critical value of energy dissipation rate, m^2/s^3
λ	relaxation time, s
μ	viscosity, Pa s

μ_0	apparent viscosity at zero shear rate, Pa s
μ_∞	apparent viscosity an infinity shear rate, Pa s
ν	kinematic viscosity, m ² /s
ξ_0	value of m_0 source term, 1/s
ϕ	suspension volume fraction, –
ρ	density, kg/m ³
σ	tensile strength, Pa

ACKNOWLEDGMENTS

This work was supported by ICHEMAD–Profarb sp. z o.o. ICHEMAD–Profarb sp. z o.o. has implemented a project entitled “Development of utility models for the construction of a set of energy-saving devices for the chemical industry, in particular for the production of paints and varnishes” under Measure 1.1.1 of the Intelligent Development Operational Program 2014-2020 co-financed by the European Regional Development Fund. This study was funded by the “Material Technologies 2 ADVANCED” project of the Warsaw University of Technology under the program Excellence Initiative: Research University. Radosław Krzosa also acknowledges the financial support received from the IDUB project (Scholarship Plus programme).

REFERENCES

- Atiemo-Obeng V.A., Calabrese R.V., 2004. Rotor–stator mixing devices, In: Paul E.L., Atiemo-Obeng V.A., Kresta S.M. (Eds.), *Handbook of industrial mixing*. DOI: [10.1002/0471451452.ch8](https://doi.org/10.1002/0471451452.ch8).
- Bałdyga J., Makowski Ł., Orciuch W., Sauter C., Schuchmann H.P., 2008a. Deagglomeration processes in high-shear devices. *Chem. Eng. Res. Des.*, 86, 1369–1381. DOI: [10.1016/j.cherd.2008.08.016](https://doi.org/10.1016/j.cherd.2008.08.016).
- Bałdyga J., Orciuch W., Makowski Ł., Malik K., Özcan-Taşkın G., Eagles W., Padron G., 2008b. Dispersion of nanoparticle clusters in a rotor-stator mixer. *Ind. Eng. Chem. Res.*, 47, 3652–3663. DOI: [10.1021/ie070899u](https://doi.org/10.1021/ie070899u).
- Bałdyga J., Orciuch W., Makowski Ł., Malski-Brodzicki M., Malik K., 2007. Break up of nano-particle clusters in high-shear devices. *Chem. Eng. Process. Process Intensif.*, 46, 851–861. DOI: [10.1016/j.cep.2007.05.016](https://doi.org/10.1016/j.cep.2007.05.016).
- Boverhof D.R., Bramante C.M., Butala J.H., Clancy S.F., Lafranconi W.M., West J., Gordon S.C., 2015. Comparative assessment of nanomaterial definitions and safety evaluation considerations. *Regul. Toxicol. Pharm.*, 73, 137–150. DOI: [10.1016/j.yrtph.2015.06.001](https://doi.org/10.1016/j.yrtph.2015.06.001).
- Chung C.J., Lin H.I., Tsou H.K., Shi Z.Y., He J.L., 2008. An antimicrobial TiO₂ coating for reducing hospital-acquired infection. *J. Biomed. Mater. Res. Part B*, 85b, 220–224. DOI: [10.1002/jbm.b.30939](https://doi.org/10.1002/jbm.b.30939).
- Fujishima A., Rao T.N., Tryk D.A., 2000. Titanium dioxide photocatalysis. *J. Photochem. Photobiol., C*, 1, 1–21. DOI: [10.1016/S1389-5567\(00\)00002-2](https://doi.org/10.1016/S1389-5567(00)00002-2).
- Gajović A., Stubičar M., Ivanda M., Furi K., 2001. Raman spectroscopy of ball-milled TiO₂. *J. Mol. Struct.*, 563–564, 315–320. DOI: [10.1016/S0022-2860\(00\)00790-0](https://doi.org/10.1016/S0022-2860(00)00790-0).
- Gavi E., Kubicki D., Padron G.A., Özcan-Taşkın N.G., 2018. Breakup of nanoparticle clusters using Microfluidizer M110-P. *Chem. Eng. Res. Des.*, 132, 902–912. DOI: [10.1016/j.cherd.2018.01.011](https://doi.org/10.1016/j.cherd.2018.01.011).
- Gázquez M.J., Bolívar J.P., Garcia-Tenorio R., Vaca F., 2014. A review of the production cycle of titanium dioxide pigment. *Mater. Sci. Appl.*, 5, 441–458. DOI: [10.4236/msa.2014.57048](https://doi.org/10.4236/msa.2014.57048).
- Hansen S., Khakhar D.V., Ottino J.M., 1998. Dispersion of solids in nonhomogeneous viscous flows. *Chem. Eng. Sci.*, 53, 1803–1817. DOI: [10.1016/S0009-2509\(98\)00010-4](https://doi.org/10.1016/S0009-2509(98)00010-4).
- Hass G., 1952. Preparation, properties and optical applications of thin films of titanium dioxide. *Vacuum*, 2, 331–345. DOI: [10.1016/0042-207X\(52\)93783-4](https://doi.org/10.1016/0042-207X(52)93783-4).

- Kamaly S.W., Tarleton A.C., Özcan-Taşkın N.G., 2017. Dispersion of clusters of nanoscale silica particles using batch rotor-stators. *Adv. Powder Technol.*, 28, 2357–2365. DOI: [10.1016/j.appt.2017.06.017](https://doi.org/10.1016/j.appt.2017.06.017).
- Krzosa R., Makowski Ł., Orciuch W., Adamek R., 2021. Population balance application in TiO₂ particle deagglomeration process modeling. *Energies*, 14, 3523. DOI: [10.3390/en14123523](https://doi.org/10.3390/en14123523).
- Mandzy N., Grulke E., Druffel T., 2005. Breakage of TiO₂ agglomerates in electrostatically stabilized aqueous dispersions. *Powder Technol.*, 160, 121–126. DOI: [10.1016/j.powtec.2005.08.020](https://doi.org/10.1016/j.powtec.2005.08.020).
- Marchisio D.L., Fox R.O., 2005. Solution of population balance equations using the direct quadrature method of moments. *J. Aerosol Sci.*, 36, 43–73. DOI: [10.1016/j.jaerosci.2004.07.009](https://doi.org/10.1016/j.jaerosci.2004.07.009).
- Marchisio D.L., Vigil R.D., Fox R.O., 2003. Quadrature method of moments for aggregation-breakage processes. *J. Colloid Interface Sci.*, 258, 322–334. DOI: [10.1016/S0021-9797\(02\)00054-1](https://doi.org/10.1016/S0021-9797(02)00054-1).
- Martínez-de Jesús G., Ramírez-Muñoz J., García-Cortés D., Cota L.G., 2018. Computational fluid dynamics study of flow induced by a grooved high-shear impeller in an unbaffled tank. *Chem. Eng. Technol.*, 41, 580–589. DOI: [10.1002/ceat.201700091](https://doi.org/10.1002/ceat.201700091).
- McGraw R., 1997. Description of aerosol dynamics by the quadrature method of moments. *Aerosol Sci. Technol.*, 27, 255–265. DOI: [10.1080/02786829708965471](https://doi.org/10.1080/02786829708965471).
- Meacock G., Taylor K.D.A., Knowles M.J., Himonides A., 1997. The improved whitening of minced cod flesh using dispersed titanium dioxide. *J. Sci. Food Agric.*, 73, 221–225. DOI: [10.1002/\(SICI\)1097-0010\(199702\)73:2<221::AID-JSFA708>3.0.CO;2-U](https://doi.org/10.1002/(SICI)1097-0010(199702)73:2<221::AID-JSFA708>3.0.CO;2-U).
- Middlemas S., Fang Z.Z., Fan P., 2015. Life cycle assessment comparison of emerging and traditional Titanium dioxide manufacturing processes. *J. Clean. Prod.*, 89, 137–147. DOI: [10.1016/j.jclepro.2014.11.019](https://doi.org/10.1016/j.jclepro.2014.11.019).
- Mikulášek P., Wakeman R.J., Marchant J.Q., 1997. The influence of pH and temperature on the rheology and stability of aqueous titanium dioxide dispersions. *Chem. Eng. J.*, 67, 97–102. DOI: [10.1016/S1385-8947\(97\)00026-0](https://doi.org/10.1016/S1385-8947(97)00026-0).
- Özcan-Taşkın N.G., Padron G., Voelkel A., 2009. Effect of particle type on the mechanisms of break up of nanoscale particle clusters. *Chem. Eng. Res. Des.*, 87, 468–473. DOI: [10.1016/j.cherd.2008.12.012](https://doi.org/10.1016/j.cherd.2008.12.012).
- Özcan-Taşkın N.G., Padron G.A., Kubicki D., 2016. Comparative performance of in-line rotor-stators for deagglomeration processes. *Chem. Eng. Sci.*, 156, 186–196. DOI: [10.1016/j.ces.2016.09.023](https://doi.org/10.1016/j.ces.2016.09.023).
- Randolph A.D., Larson M.A., 1962. Transient and steady state size distributions in continuous mixed suspension crystallizers. *AIChE J.*, 8, 639–645. DOI: [10.1002/aic.690080515](https://doi.org/10.1002/aic.690080515).
- Reck E., Richards M., 1999. TiO₂ manufacture and life cycle analysis. *Pigm. Resin Technol.*, 28, 149–157. DOI: [10.1108/03699429910271297](https://doi.org/10.1108/03699429910271297).
- Rodgers T.L., Cooke M., Siperstein F.R., Kowalski A., 2009. Mixing and dissolution times for a cowles disk agitator in large-scale emulsion preparation. *Ind. Eng. Chem. Res.*, 48, 6859–6868. DOI: [10.1021/ie900286s](https://doi.org/10.1021/ie900286s).
- Sen S., Ram M.L., Roy S., Sarkar B.K., 1999. The structural transformation of anatase TiO₂ by high-energy vibrational ball milling. *J. Mater. Res.*, 14, 841–848. DOI: [10.1557/JMR.1999.0112](https://doi.org/10.1557/JMR.1999.0112).
- Shamlou P.A., Titchener-Hooker N., 1993. Turbulent aggregation and breakup of particles in liquids in stirred vessels, In: Shamlou P.A. (Ed.), *Processing of Solid-Liquid Suspensions*. Butterworth-Heinemann Ltd. 1–25. DOI: [10.1016/b978-0-7506-1134-3.50005-3](https://doi.org/10.1016/b978-0-7506-1134-3.50005-3).
- Tang S., Ma Y., Shiu C., 2001. Modelling the mechanical strength of fractal aggregates. *Colloids Surf., A*, 180, 7–16. DOI: [10.1016/S0927-7757\(00\)00743-3](https://doi.org/10.1016/S0927-7757(00)00743-3).
- Unadkat H., Rielly C.D., Nagy Z.K., 2011. PIV study of the flow field generated by a sawtooth impeller. *Chem. Eng. Sci.*, 66, 5374–5387. DOI: [10.1016/j.ces.2011.07.046](https://doi.org/10.1016/j.ces.2011.07.046).
- Weir A., Westerhoff P., Fabricius L., Hristovski K., Von Goetz N., 2012. Titanium dioxide nanoparticles in food and personal care products. *Environ. Sci. Technol.*, 46, 2242–2250. DOI: [10.1021/es204168d](https://doi.org/10.1021/es204168d).
- Xie L., Rielly C.D., Eagles W., Özcan-Taşkın G., 2007. Dispersion of nano-particle clusters using mixed flow and high shear impellers in stirred tanks. *Chem. Eng. Res. Des.*, 85, 676–684. DOI: [10.1205/cherd06195](https://doi.org/10.1205/cherd06195).

R. Krzosa, K. Wojtas, J. Golec, Ł. Makowski, W. Orciuch, R. Adamek, *Chem. Process Eng.*, 2021, 42 (2), 105–118

Xie L., Rielly C.D., Özcan-Taskin G., 2008. Break-Up of nanoparticle agglomerates by hydrodynamically limited processes. *J. Dispers. Sci. Technol.*, 29, 573–579. DOI: [10.1080/01932690701729211](https://doi.org/10.1080/01932690701729211).

Yang H.G., Li C.Z., Gu H.C., Fang T.N., 2001. Rheological behavior of titanium dioxide suspensions. *J. Colloid Interface Sci.*, 236, 96–103. DOI: [10.1006/jcis.2000.7373](https://doi.org/10.1006/jcis.2000.7373).

Yu J., Zhao X., Zhao Q., Wang G., 2001. Preparation and characterization of super-hydrophilic porous TiO₂ coating films. *Mater. Chem. Phys.*, 68, 253–259 DOI: [10.1016/S0254-0584\(00\)00364-3](https://doi.org/10.1016/S0254-0584(00)00364-3).

Zhang J., Xu S., Li W., 2012. High shear mixers: A review of typical applications and studies on power draw, flow pattern, energy dissipation and transfer properties. *Chem. Eng. Process.*, 57–58, 25–41. DOI: [10.1016/j.cep.2012.04.004](https://doi.org/10.1016/j.cep.2012.04.004).

Received 11 June 2021

Received in revised form 29 July 2021

Accepted 2 August 2021